

Topological Charge Inversion of Optical Vortex with Geometric Metasurfaces

Yuchao Zhang, Jie Gao,* and Xiaodong Yang*

The topological charge (TC) inversion of optical vortex is demonstrated along the beam propagation direction by using plasmonic geometric metasurfaces with the initial wave fronts designed from the principle of caustic surface. The detailed TC inversion evolution process is observed together with the transmutation point where the vortex vanishes. The orbital angular momentum (OAM) mode distributions during the TC inversion process are studied to show the dynamic redistributions of OAM mode density between the central area and the surrounding area of the beam with the total OAM conserved. Furthermore, the TC inversion of self-accelerating vortex beam along the parabolic trajectory is presented. The realization of controlling TC inversion of optical vortex along arbitrary beam trajectory paves the way for many applications with more complex functionalities in optical trapping and manipulation, optical sensing, quantum information and computation, and data communication.

1. Introduction

Optical vortex beams with screw phase dislocations have raised extensive attention due to their unique characteristics of phase singularities in light beam carrying orbital angular momentum (OAM), enabling a wide variety of applications such as optical trapping of atoms,^[1–3] optical communication,^[4,5] quantum information and computation,^[6–9] spin–orbit OAM transformation,^[10,11] and Bose–Einstein condensates and superfluids.^[12,13] The helix phase structure of optical vortex can be represented in the form of $\exp(il\varphi)$, where φ is the azimuthal angle around the phase singularity, and l represents the topological charge (TC). As the most essential parameter of optical vortex, TC describes the phase increase around the vortex center and plays an important role in applications. For example, in quantum information processing, TC is used for data encoding and decoding, while in optical manipulation, TC controls the strength and sign of the optical torque applied on particles. For a well-defined Laguerre–Gaussian (LG) beam, the TC represents the OAM of photons and it should keep invariant as the beam propagates in free space due to the OAM conservation law.^[14] Recently,

dynamic TC inversion has been realized with the noncanonical optical vortex by using an astigmatic lens,^[15,16] showing the OAM is a superposition of LG modes with different charges and the OAM mode density can be dynamically redistributed across the beam. In this case, the total OAM value is kept constant, but the local OAM mode density is changed. However, this method to generate TC inversion of optical vortex requires the noncanonical phase distribution and the conversion from an astigmatic lens, which increases the optical system complexity and also limits the photonic chip integration. Besides, the generated TC inversion beam has an irregular intensity profile and it is hard to control the transmutation point and beam propagation trajectory.

Recently, plasmonic metasurfaces made of nanoantenna arrays in ultrathin metallic films have provided a powerful and functional platform for tailoring the phase, intensity, and polarization of light.^[17–19] The transmission efficiency of plasmonic metasurfaces is relatively low due to the large ohmic loss of metal. In order to solve this problem, dielectric metasurfaces made of silicon or titanium oxide have been considered to manipulate light with ultrahigh efficiency.^[20–22] In particular, geometric metasurfaces can be engineered to generate well-defined Pancharatnam–Berry geometric phase profiles in a broad wavelength range,^[23–27] for building on-chip wavefront shaping devices such as optical vortex generators,^[28–32] flat optical lenses,^[33–38] compact wave plates,^[39–42] and multiplexed holograms.^[43–47] In addition, holographic free-electron light source based on plasmonic metasurfaces has been realized for generation of visible to near-infrared vortex beams.^[48]

In this work, the TC inversion of optical vortex beam is demonstrated along the beam propagation direction by using the ultrathin plasmonic metasurfaces constructed from nanoslit antenna arrays with the geometric phase profiles designed from the principle of caustic surface. Compared to the previous work, the proposed approach to realize TC inversion of optical vortex provides the controllable optical vortex transformation along an arbitrary beam trajectory. Besides, only a single metasurface with compact size is utilized to realize the TC inversion, which is convenient for integration into optical systems. The detailed TC inversion evolution process is observed including the predesigned transmutation point in a broad wavelength range. The dynamic redistribution of OAM mode density between the central area of $r < 10 \mu\text{m}$ and the surrounding

Dr. Y. Zhang, Prof. J. Gao, Prof. X. Yang
Department of Mechanical and Aerospace Engineering
Missouri University of Science and Technology
Rolla, MO 65409, USA
E-mail: gaojie@mst.edu; yangxia@mst.edu

The ORCID identification number(s) for the author(s) of this article can be found under <https://doi.org/10.1002/adom.201801486>.

DOI: 10.1002/adom.201801486

area of $r > 10 \mu\text{m}$ of the beam is also analyzed according to the simulated OAM mode distributions, while the total OAM across the beam is conserved. In addition, the TC inversion of self-accelerating vortex beam along the parabolic trajectory is presented. Our demonstrated results will pave the way for many promising applications in optical trapping and manipulation, optical sensing, quantum information and computation, and data communication.

2. Results and Discussion

2.1. Design of Plasmonic Geometric Metasurface

As shown in Figure 1a, each unit cell of the plasmonic geometric metasurface contains a nanoslit antenna with a certain orientation angle. The nanoslit antennas are etched in a thin gold film with thickness of 50 nm on glass substrate using focused ion beam (FIB) method. The width and length of each nanoslit antenna are 80 and 200 nm, respectively, and the unit cell period is 330 nm. When a circularly polarized beam transmits through the nanoslit antenna with orientation angle θ , the induced geometric phase shift of 2θ is introduced to the converted spin component. The desired geometric phase profile of the metasurface is then obtained by arranging the nanoslit antennas with the designed rotation angles to form a spatially inhomogeneous array. Figure 1b is the simulated electric field $|E|$ distributions

for the right-handed and left-handed circular polarizations (RCP and LCP), with the observed strong polarization anisotropy. The scanning electron microscope (SEM) image of the fabricated homogeneous array of nanoslit antennas is shown in Figure 1c. For the transmission under circular polarization basis, the incident beam has LCP and the total transmitted beam through the metasurface contains both the LCP (original spin) component and the RCP (converted spin) component. The original spin transmission is defined as the intensity ratio between the transmitted LCP component and the incident LCP beam, while the converted spin transmission is defined as the intensity ratio between the converted RCP component and the incident LCP beam. The polarization conversion efficiency (CE) is defined as the intensity ratio between the converted spin component and the total transmitted beam. Figure 1d plots the measured and simulated spectra of original spin transmission (LCP, green line), converted spin transmission (RCP, blue line), and CE (red line). The converted RCP transmission is between 1% and 5%. The observed maximum conversion efficiency is around 55% near 800 nm, where the plasmonic resonance occurs.

Previously, caustic curves along arbitrary convex trajectories have been realized with the geometrical optics method based on the conical ray bundles emitted from circles on the input wavefront plane.^[49] Here, the geometric phase profile encoded on the plasmonic metasurface is designed from the principle of caustic surface for demonstrating the TC inversion of optical vortex. The initial field profile located on the input plane of

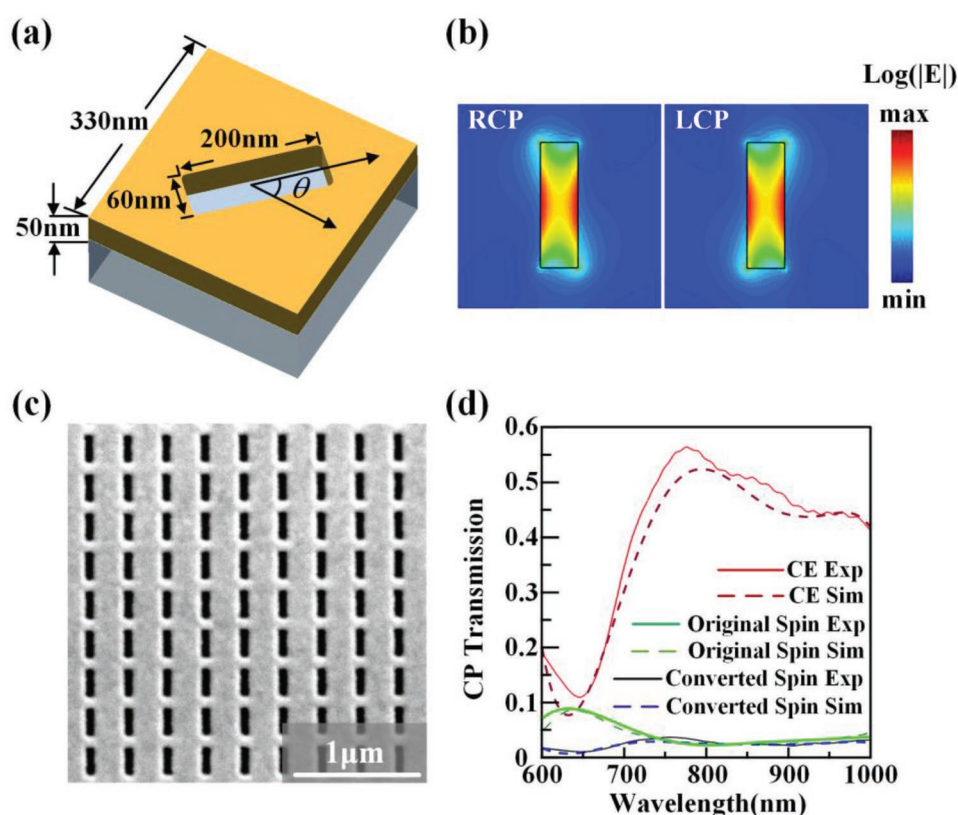


Figure 1. a) Schematic of the unit cell design of the nanoslit antenna at orientation angle of θ . b) Simulated electric field $|E|$ distributions of nanoslit antenna under circular polarizations at 633 nm. c) An SEM image of the fabricated homogeneous nanoslit antenna array. d) Measured and simulated transmission spectra and conversion efficiency spectra under circular polarization basis.

$z = 0$ is defined as $\Psi(x_0, y_0, z = 0) = G(r_0) \exp(ikQ(x_0, y_0))$, where the initial wave front $\varphi_{\text{geom}} = kQ(x_0, y_0)$ represents the geometric phase shift from the metasurface and k is the wavenumber. The optical field at the propagation distance z can be obtained by the Fresnel diffraction formula

$$\Psi(x, y, z) = \iint \frac{dx_0 dy_0}{i\lambda z} G(r_0) \exp \left\{ ik \left[Q(x_0, y_0) + \frac{(x - x_0)^2 + (y - y_0)^2}{2z} \right] \right\} \quad (1)$$

Based on the stationary phase approach, the integration in Equation (1) is mainly determined by the critical points that fulfill the two conditions of $(x - x_0)/z = dQ/dx_0$ and $(y - y_0)/z = dQ/dy_0$. Then, the caustic curve along the beam propagation direction can be parametrically expressed as $[f(z), g(z), z]$. As shown in **Figure 2a**, one point with the fixed $z = z'$ parameter on the caustic curve corresponds to a circle $C(z = z')$ on the input plane and a conical ray bundle emitted from this circle will intersect at this point. As the z parameter changes, the formed continuous caustic is the locus of the apexes of the conical ray bundles emitted from the expanding and shifting circles on the input plane,^[49] as shown in the red line of **Figure 2a**. The circle function of $C(z)$ is expressed as

$(x_0 - x_c)^2 + (y_0 - y_c)^2 = R(z)^2$, where x_c and y_c are the center of the circle defined by $x_c = f - zf'$ and $y_c = g - zg'$, and the radius $R(z)$ is used to control the size of the circle. Such circle function relates the propagation distance z with the circle $C(z)$ on the input plane, so that the distance z can be expressed as the function of the point on the initial plane, $z = z(x_0, y_0)$. When there is no optical vortex contained in the initial beam, the conical ray bundle emitted from $C(z)$ will be focused into the point $[f(z), g(z), z]$, and the initial function $Q(x_0, y_0)$ is given by

$$Q(x_0, y_0) = \frac{1}{2} \int_0^z \left\{ [f'(\xi)]^2 + [g'(\xi)]^2 - \left[\frac{R(\xi)}{\xi} \right]^2 \right\} d\xi - \frac{(f - x_0)^2 + (g - y_0)^2}{2z} \quad (2)$$

when a vortex structure $\exp(il\varphi)$ is imposed to the initial field, the initial phase profile becomes $\exp[i(kQ + l\varphi)]$. In this case, the stationary phase condition for the Fresnel diffraction integral becomes

$$\frac{l}{k} \frac{d\varphi}{dx_0} + \frac{dQ}{dx_0} = \frac{x - x_0}{z} \quad \text{and} \quad \frac{l}{k} \frac{d\varphi}{dy_0} + \frac{dQ}{dy_0} = \frac{y - y_0}{z} \quad (3)$$

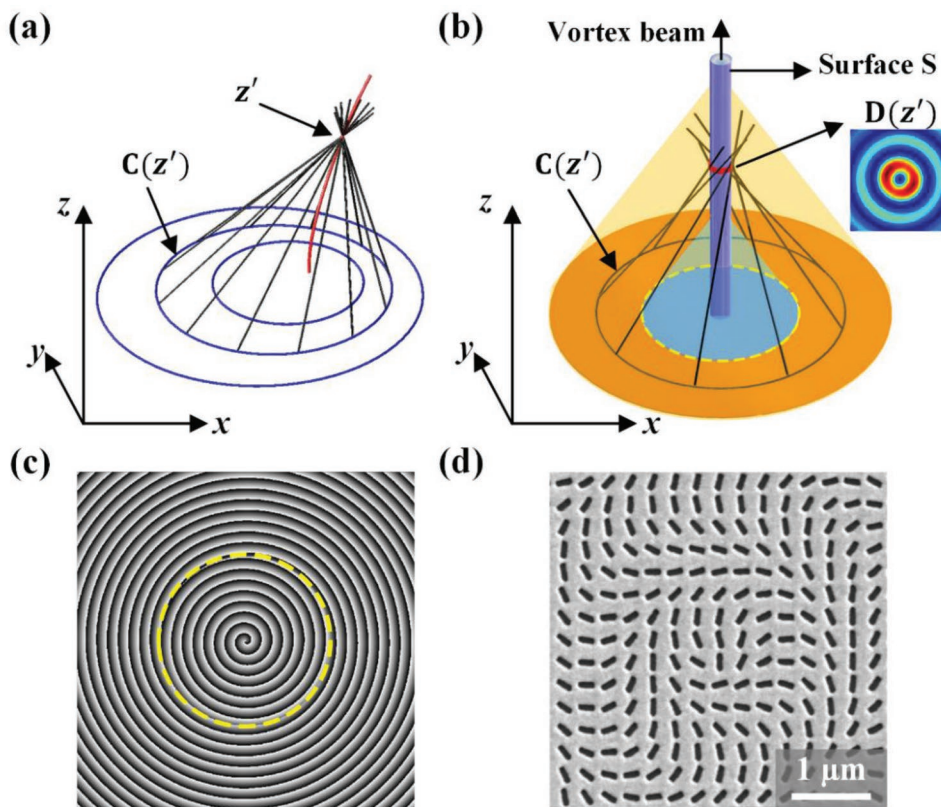


Figure 2. a) Schematic illustration of the principle of caustic curve. The conical ray bundle emitted from circle $C(z')$ intersects at a point on the plane $z = z'$, and as the circle expanding and shifting on the input plane, the intersect points form the caustic curve, as marked by the red curve. b) Schematic illustration of the principle of caustic surface with the imposed vortex structure to the initial field, where the rays emitted from circle $C(z')$ intersect in a circle $D(z')$ on the plane $z = z'$. As the circle expanding and shifting on the input plane, the intersect circles form the caustic surface S . The input plane is divided by the yellow dashed circle into inner zone with TC of -1 and outer zone with TC of $+1$. c) The geometric phase profile on the input plane encoded in the metasurface, and the yellow dashed circle divides the input plane into inner zone and outer zone. d) An SEM image of the fabricated metasurface structure corresponding to the central area in (c).

For a large wavenumber k values, the terms $ld\varphi/kdx_0$ and $ld\varphi/kdy_0$ are much smaller compared with other terms and could be neglected, so the optical field in the propagation distance z is still mainly contributed by the emanation points on the circle $C(z)$. In this case, upon using polar coordinates of $(x_0, y_0) = r_0 (\cos \varphi, \sin \varphi)$ and $(x, y) = \rho(\cos \theta, \sin \theta)$, the complex field distribution at distance z is calculated by $F(z) = \int \exp(i\ell\varphi) \exp(-ikr_0\rho \cos(\varphi - \theta)/z) d\varphi = 2\pi J_1(kr_0\rho/z) \exp(i\ell\theta)$.^[49] Therefore, at the propagation distance z , the field is a vortex field with TC or vorticity being equal to ℓ , and its intensity distribution approximately behaves like a Bessel function with order ℓ .

From the view of optical catastrophe theory, the caustics are singularities of differentiable mappings induced by the families of rays with the direction along the phase gradient. For the initial beam without vortex phase structure, the rays from circle $C(z')$ propagate along the direction $\mathbf{l} = (dQ/dx_0, dQ/dy_0)$ and intersect at the point $[f(z'), g(z'), z']$ on the caustic curve, as shown in Figure 2a. In this case, for the point on the caustic curve, there are infinite rays that cross each point, while for other points in the space, there are only two rays that cross each point. Thus, the number of the rays is discontinuity on the caustic curve (changes from 2 to ∞), and this type of abrupt change in the configuration of critical points is known as a ‘‘catastrophe.’’. After the vortex phase structure is imposed on the initial field, the direction of rays will be deflected at a small angle $\Delta\mathbf{l} = (d\varphi/dx_0, d\varphi/dy_0)/k$ with respect to the origin direction \mathbf{l} . Because the wavenumber k is very large, so the $\Delta\mathbf{l}$ imposes a small perturbation to the origin direction \mathbf{l} . As shown in Figure 2b, in this case, the rays emitted from circle $C(z')$ will pass through the points offset to the origin point $[f(z'), g(z'), z']$ on the caustic curve. The ray bundle intersects the $z = z'$ plane with a circle $D(z')$, and each ray is tangential to this circle. As the circle $C(z)$ expands and shifts on the initial plane, the generated circle $D(z)$ would move along the original caustic curve, forming a doubly ruled surface \mathbf{S} . Inside the doubly ruled surface \mathbf{S} , there is no light ray passing through, and outside the surface \mathbf{S} each point has two rays passing through, so the number of the rays entering into the surface \mathbf{S} abruptly changes from two to zero, forming a caustic surface in the physical space and a resultant optical vortex field, as shown in the inset of Figure 2b. From the above analysis, it can be concluded that at the propagation distance z the caustic optical field is mainly determined by the initial field at circle $C(z)$. If a vortex structure is imposed on the circle $C(z)$, the optical field at the distance z will have a vortex field with TC being equal to that on the circle $C(z)$. As a result, optical vortex fields with varying TC values located at different propagation distances z can be generated by different circles $C(z)$ on the input plane. As shown in Figure 2b, the input plane is separated by the yellow dashed circle into the inner zone with TC of -1 and the outer zone with TC of $+1$. Then the $C(z)$ in the inner zone will produce the vortex with TC of -1 at the lower propagation distances, while the $C(z)$ in the outer zone will create the vortex with TC of $+1$ at the higher propagation distances. The entire input plane will generate the TC inversion beam. The dividing line of the yellow dashed circle corresponds to a propagation distance z_T named as the transmutation point of the TC inversion process.

In this work, both the TC inversion of optical vortex beam propagating along the straight line and the TC inversion of

self-accelerating vortex beam following the parabolic trajectory are demonstrated. For the first case, the straight line can be expressed as the parameter functions of z , $[f(z) = 0, g(z) = 0, z]$. Next, a function $L(z)$ is introduced to describe the vortex TC at different distances with $L(z) = \{-1, z \leq z_T; 1, z > z_T\}$, where $z_T = 50 \mu\text{m}$ is the transmutation point of the TC inversion. The initial phase distribution is obtained by substituting the parameter functions of caustic curve $f(z)$ and $g(z)$ into Equation (2) to calculate the function $Q(x_0, y_0)$ and then adding the vortex phase structure $\exp[iL(z)\varphi]$ to kQ . The total geometric phase profile on the input plane encoded in the metasurface is

$$\varphi_{\text{geom}}(x, y) = kQ(x_0, y_0) + L[z(x_0, y_0)] \arctan(y_0/x_0) \quad (4)$$

where the wavenumber is $k = 2\pi/\lambda$ and the function $z(x_0, y_0)$ is deduced from the circle function $(x_0 - x_c)^2 + (y_0 - y_c)^2 = R(z)^2$. For the vortex beam propagates along the straight line, $f = g = f' = g' = 0$, so that $x_c = f - z f' = 0$ and $y_c = g - z g' = 0$. As the radius function $R(z)$ is chosen to be $R(z) = z/3$, the corresponding circle function is $x_0^2 + y_0^2 = z^2/9$ and thus $z = 3\sqrt{x_0^2 + y_0^2}$. On substituting these results into Equation (2), the function $Q(x_0, y_0) = -\sqrt{(x_0^2 + y_0^2)}/3$ is obtained. At the wavelength $\lambda = 0.633 \mu\text{m}$, the wavenumber $k = 9.9$, so that the total geometric phase could be derived by employing Equation (4)

$$\varphi_{\text{geom}} = -3.3\sqrt{(x_0^2 + y_0^2)} + L(z) \arctan(y_0/x_0) \quad (5)$$

with $z = 3\sqrt{x_0^2 + y_0^2}$, as displayed in Figure 2c. Finally, the metasurface is formed by rotating the nanoslit antenna within each unit cell with the orientation angle $\theta(x_0, y_0)$ determined by half of the transmitted geometric phase shift as $\theta(x_0, y_0) = \varphi_{\text{geom}}(x_0, y_0)/2$. The SEM image of the fabricated metasurface structure is shown in Figure 2d, corresponding to the central area of the phase distribution in Figure 2c.

2.2. TC Inversion of Optical Vortex Beam

The TC inversion process of optical vortex from -1 to $+1$ is first simulated using the Fresnel–Kirchhoff integral. Figure 3a,b displays the evolution processes of the intensity distributions and phase profiles at the propagation distance $z = 30 \mu\text{m}$, $z = 40 \mu\text{m}$, $z = 50 \mu\text{m}$, $z = 60 \mu\text{m}$, and $z = 70 \mu\text{m}$, respectively. At $z = 30 \mu\text{m}$, the intensity distribution has a well-defined Bessel-like pattern and its phase profile shows one vortex structure with TC of -1 located at the center, with counter-clockwise-increased helical phase. At $z = 40 \mu\text{m}$, the Bessel-like intensity pattern is deformed and the main lobe of ring-shaped pattern is divided into two connected lobes. For the phase profile at $z = 40 \mu\text{m}$, besides the central vortex structure, there are other phase defects presenting near the central vortex. At $z = 50 \mu\text{m}$, it can be seen that the intensity pattern completely becomes two nonconnected lobes, and the central vortex structure in the phase profile completely vanishes, indicating the transmutation point z_T of the TC inversion process. At $z = 60 \mu\text{m}$, the intensity pattern resumes the shape of two connected lobes, which is similar to the pattern at $z = 40 \mu\text{m}$, but the phase profile shows a central vortex structure with the clockwise-increased helical

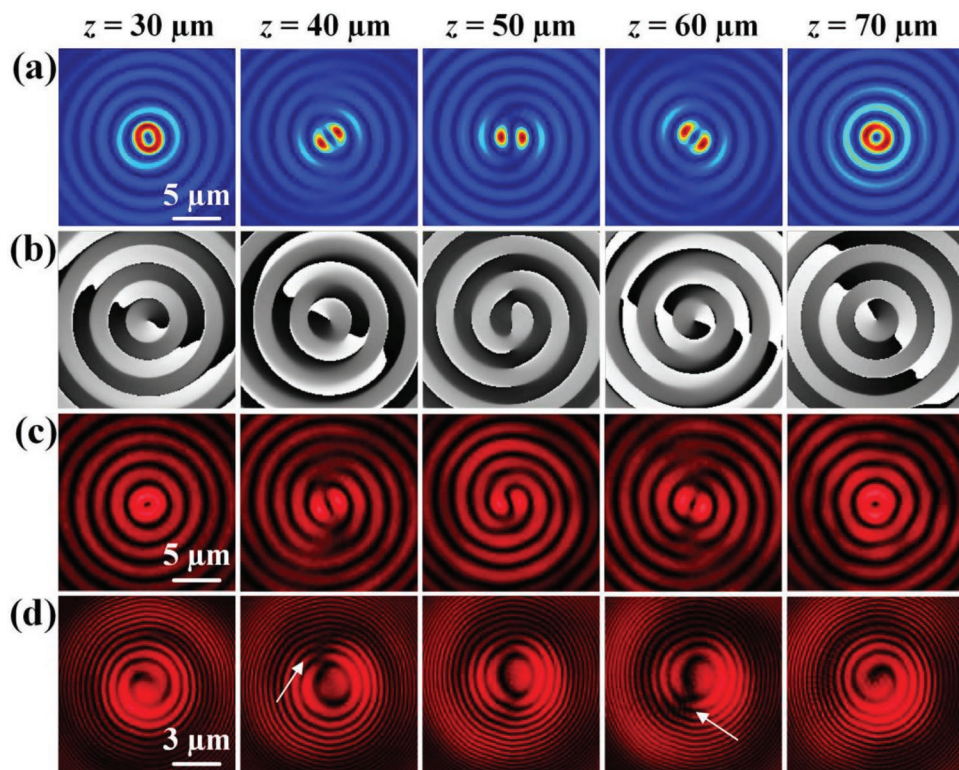


Figure 3. a) Simulated cross-sectional intensity distributions and b) the corresponding phase profiles for the TC inversion process at the propagation distances of $z = 30 \mu\text{m}$, $z = 40 \mu\text{m}$, $z = 50 \mu\text{m}$, $z = 60 \mu\text{m}$, and $z = 70 \mu\text{m}$. c) Measured intensity distributions at the wavelength of 633 nm at different propagation distances. d) Measured interferometry patterns of TC inversion beam interfered with a spherical wave, and the white arrow indicates the phase discontinuous cut line.

phase. Also some phase defects present near the central vortex. At $z = 70 \mu\text{m}$, the intensity pattern is completely changed into the regular Bessel-like ring-shaped pattern again and its phase profile shows the vortex structure with TC of +1 at the center.

The TC inversion evolution process from -1 to $+1$ is then observed from the fabricated metasurface at the wavelength of 633 nm. Figure 3c shows the measured intensity distributions at different propagation distances, and Figure 3d plots the corresponding interferometry patterns interfered with a spherical wave. It is shown that the evolution process of the intensity patterns is coincident with the simulated results, including the regular Bessel-like ring-shaped pattern, two connected lobes, and two nonconnected lobes at different propagation distances. At $z = 30 \mu\text{m}$ and $z = 70 \mu\text{m}$, the interference fringes show well-defined spirals with counterclockwise rotation at $z = 30 \mu\text{m}$ and clockwise rotation at $z = 70 \mu\text{m}$, suggesting the optical vortices with the inverted TCs from -1 to $+1$. At $z = 40 \mu\text{m}$, a phase discontinuous cut line containing a vortex chain with alternating charge of $+1$ and -1 is presented along one radial direction, which shows the TC has a fractional value between -1 and 0 . While at $z = 60 \mu\text{m}$, a phase edge dislocation appears again along one radial direction, showing the TC with a fractional value between 0 and $+1$. At $z = 50 \mu\text{m}$, the interferometry ring structures are continuous without any spiral structure, giving the TC of 0 .

It should be emphasized that in our approach the beam propagates completely in free space, thus this TC inversion

process does not involve any wave front dislocation induced by external discontinuities. Therefore, according to the angular momentum conservation law, the OAM should keep invariant.^[14] However, the TC inversion beam is not a pure Laguerre–Gaussian mode with the defined OAM state, so here we decompose the beam into the superposition of Laguerre–Gaussian modes carrying different TCs, as shown in Figure 4. In this figure, the mode weight is calculated by the formula: $c_m = \langle m | F(r, \varphi) \rangle = \iint F(r, \varphi) \exp(-im\varphi) r dr d\varphi$, where $F(r, \varphi)$ represents the field distributions and $|m\rangle = \exp(im\varphi)$ is the eigenfunction of the angular momentum operator $-i\partial/\partial\varphi$.^[50] The left figure in Figure 4 plots the total OAM mode distribution, showing that the mode distribution for this TC inversion beam is mainly contributed by the $|l = -1\rangle$ and $|l = +1\rangle$ states. The total OAM mode distribution is conserved at different propagation distances, so the TC inversion process does not conflict with the OAM conservation law. Although the total OAM is kept invariant, the OAM mode density is dynamically redistributed across the beam during its evolution. In Figure 4, the dynamic OAM mode redistributions between the central area of $r < 10 \mu\text{m}$ (top row) and the surrounding area of $r > 10 \mu\text{m}$ (bottom row) of the beam are plotted. In the inner zone, at $z = 30 \mu\text{m}$ the OAM is mainly constituted by $|l = -1\rangle$ state, and at $z = 40 \mu\text{m}$ the weight of $|l = +1\rangle$ state increases but is still smaller than $|l = -1\rangle$ state. At the transmutation point $z_T = 50 \mu\text{m}$, the weight of $|l = -1\rangle$ state and $|l = +1\rangle$ state have almost the same value in the central area. At $z = 60 \mu\text{m}$, the

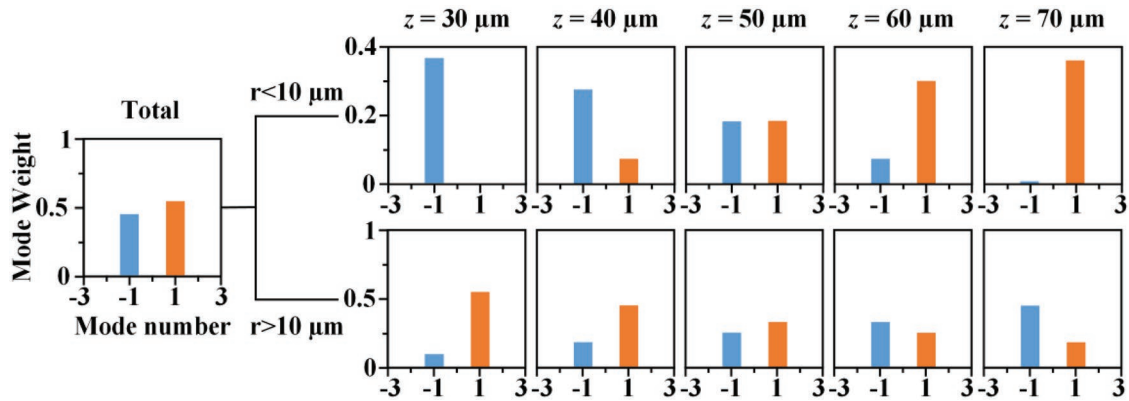


Figure 4. The calculated OAM mode distributions of the TC inversion beam at different propagation distances. The left figure is the total OAM mode and the top row and bottom row in the right figure represent the dynamic OAM mode redistributions within the central area of $r < 10 \mu\text{m}$ and the surrounding area of $r > 10 \mu\text{m}$ of the beam.

weight of $|l = +1\rangle$ state increases and is larger than the weight of $|l = -1\rangle$ state, and finally at $z = 70 \mu\text{m}$ the OAM is mainly constituted by $|l = +1\rangle$ state in the central area. During the evolution of TC inversion from $|l = -1\rangle$ to $|l = +1\rangle$, the OAM mode in the central area changes from $|l = -1\rangle$ state to $|l = +1\rangle$ state, and at the transmutation point these two states have the same weight. The OAM states in the outer zone also change accordingly to keep the total OAM across the beam conserved. This dynamic redistribution of OAM mode density will benefit many applications based on OAM states such as quantum information processing and data communication. In order to minimize the side effects in practical applications, the generated TC inversion beam can be further spatially filtered by a pinhole, or directly coupled into a single-mode optical fiber or a specific air-core fiber with diameter of several micrometers.^[51,52]

The broadband response of the metasurface is also demonstrated. **Figure 5** shows the measured intensity distributions of TC inversion beam at the wavelength of 808 and 988 nm at different propagation distances. As the wavelength changes, the corresponding transmutation point is varied according to the relationship $z_T(\lambda_2) = z_T(\lambda_1) \cdot \lambda_2 / \lambda_1$, which is derived from the change of Fresnel propagation phase in Equation (1), so the transmutation point for 808 and 988 nm is around 60 and 80 μm , respectively. It is shown that the measured

evolution processes of TC inversion at 808 and 988 nm are almost the same as that at 633 nm, indicating the broadband operation capabilities of the metasurface.

2.3. TC Inversion of Self-Accelerating Vortex Beam

The TC inversion of self-accelerating optical vortex beam propagating along the parabolic trajectory is further demonstrated. For the parabolic trajectory, the parameter function of parabolic curve is $[f(z) = z^2/900, g(z) = 0, z]$, and the TC function is chosen as $L(z) = \{-1, z \leq z_T; +1, z > z_T\}$, where $z_T = 100 \mu\text{m}$. In this case, $f' = z/450, g' = 0, x_c = f - z f' = -z^2/900$, and $\gamma_c = 0$. The corresponding circle function is $(x_0 + z^2/900)^2 + \gamma_0^2 = z^2/17$, so that $z = \sqrt{(x_0 + z^2/900)^2 + \gamma_0^2}$. According to the integration of Equation (2), the function $Q(x_0, \gamma_0)$ is expressed as

$$Q(x_0, \gamma_0) = \frac{1}{2} \int_0^z \left\{ \left[\frac{z}{450} \right]^2 - \frac{1}{17} \right\} d\xi - \frac{(z^2/900 - x_0)^2 + (g - \gamma_0)^2}{2z} \quad (6)$$

$$= (z^3/35735 - z)/34 - [(z^2/900 - x_0)^2 + \gamma_0^2]/2z$$

At the wavelength $\lambda = 0.633 \mu\text{m}$, the wavenumber $k = 9.9$, so that the total geometric phase is derived from Equation (4) as

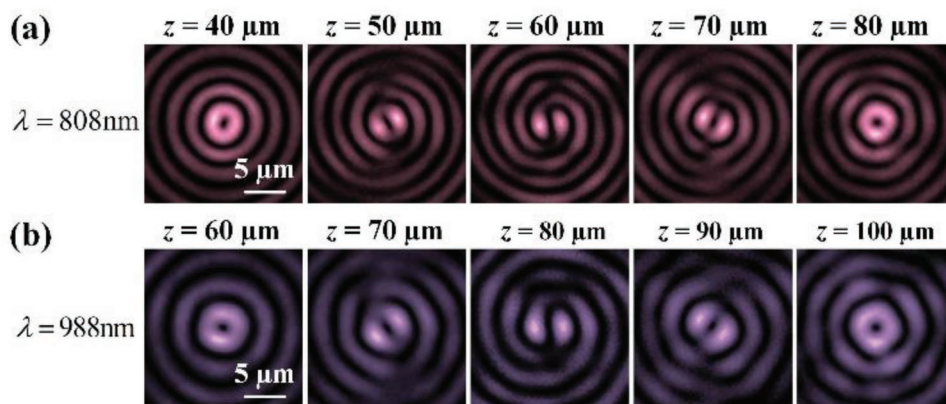


Figure 5. Measured intensity distributions at different propagation distances at the wavelength of a) 808 nm and b) 988 nm at different propagation distances.

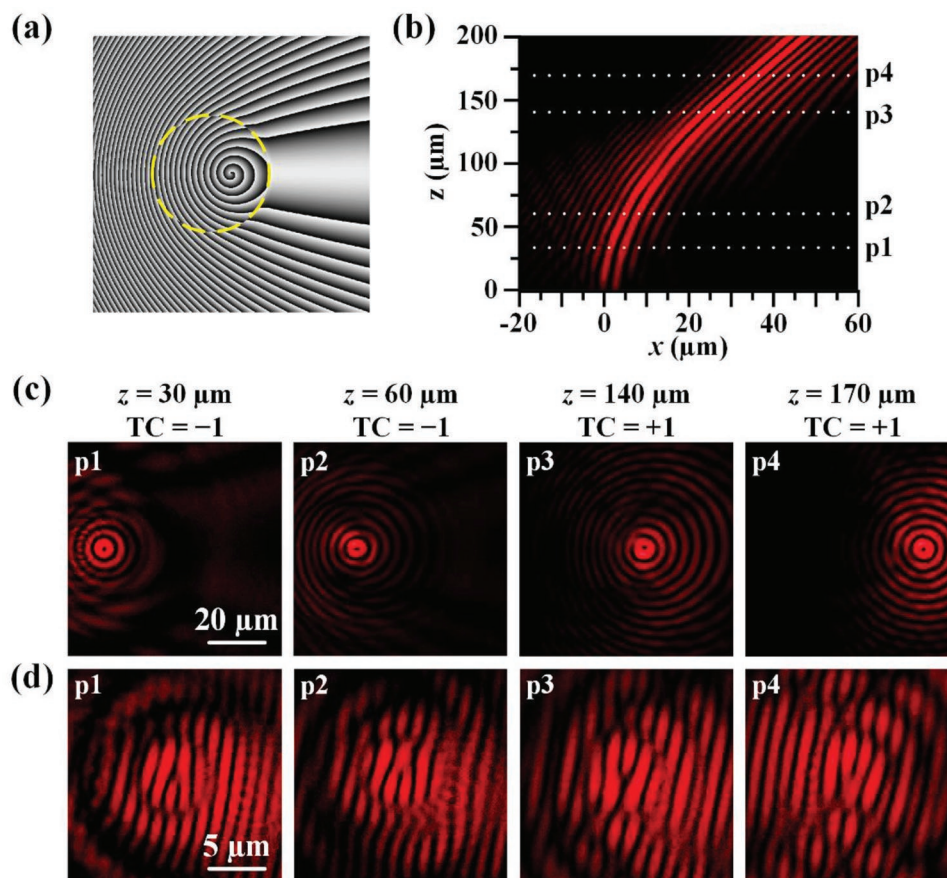


Figure 6. a) The phase profile used to generate the self-accelerating TC inversion beam propagating along the parabolic trajectory. The yellow dashed line divides the phase plane into inner zone with TC of -1 and outer zone with TC of $+1$. b) Measured intensity distribution in the x - z plane to demonstrate the evolution process of the self-accelerating TC inversion beam. c) Measured transverse intensity profiles and d) interferometry patterns at four different propagation distances (p1, p2, p3, and p4) marked by the white dotted lines in (b).

$$\varphi_{\text{geom}} = 0.3(z^3/35735 - z) - 5[(z^2/900 - x_0^2) + y_0^2]/z + L(z)\arctan(y_0/x_0) \quad (7)$$

with $z = \sqrt{(x_0 + z^2/900)^2 + y_0^2}$. **Figure 6a** shows the corresponding phase profile for the TC inversion beam with parabolic trajectory, and the yellow dashed circle in the figure divides the inner zone $\{(x_0, y_0) | z(x_0, y_0) \leq z_T\}$ and the outer zone $\{(x_0, y_0) | z(x_0, y_0) > z_T\}$, and the inner zone has TC of -1 and the outer zone has TC of $+1$.

To demonstrate the evolution process of self-accelerating TC inversion beam, the intensity distributions at the propagation distances from $z = 0 \mu\text{m}$ to $z = 200 \mu\text{m}$ at the interval of $5 \mu\text{m}$ are captured at the wavelength of 633 nm for assembling the intensity distribution along the beam propagation in the x - z plane, as plotted in **Figure 6b**. It is shown that the generated self-accelerating vortex beam follows the pre-designed parabolic trajectory and exhibits the diffraction-free behaviors. Unlike the traditional self-accelerating beam with only one main lobe along the pre-designed trajectory,^[53–55] this self-accelerating vortex beam has the doughnut-like vortex core moving along the trajectory. **Figure 6c** is the transverse intensity profiles at four different propagation distances of $z = 30 \mu\text{m}$ (p1), $z = 60 \mu\text{m}$ (p2), $z = 140 \mu\text{m}$ (p3), and $z = 170 \mu\text{m}$ (p4) for the self-acceleration TC inversion

beam with parabolic trajectory. The vortex fields at the positions of p1 and p2 with $z < 100 \mu\text{m}$ have TCs of -1 , while the vortex fields at p3 and p4 with $z > 100 \mu\text{m}$ have TCs of $+1$. It is clearly seen that the intensity profile has a Bessel-like pattern at each position and the vortex core moves from left to right. **Figure 6d** shows the corresponding interferometry patterns with the plane wave, where the interference fork fringes have downward orientation at the positions of p1 and p2 and upward orientation at the positions of p3 and p4, indicating the vortex beams have the inversed TCs from -1 at $z < 100 \mu\text{m}$ to $+1$ at $z > 100 \mu\text{m}$. Furthermore, it should be pointed out that since the self-accelerating beam propagates completely in free space and the TC inversion process does not involve any wavefront dislocation induced by external discontinuities, the OAM for the self-accelerating vortex beam is also conserved.

3. Conclusion

In summary, the TC inversion of optical vortex beam from $|l = -1\rangle$ state to $|l = +1\rangle$ state in free space has been demonstrated along arbitrary beam trajectory by using the plasmonic geometric metasurfaces made of nanoslit antenna arrays with the initial phase profiles designed from the principle of

caustic surface. The detailed TC inversion evolution process is observed with the predefined transmutation point where the vortex structure vanishes. The dynamic redistribution of OAM mode density between the central area of $r < 10 \mu\text{m}$ and the surrounding area of $r > 10 \mu\text{m}$ of the beam is also analyzed according to the simulated OAM mode distributions, with the conserved total OAM across the beam. The TC inversion of self-accelerating vortex beam along the parabolic trajectory is further demonstrated. Such demonstrated TC inversion beams will be useful for a wide range of applications with more complex functionality and performance, especially in optical trapping and manipulation, optical sensing, quantum information and computation, and data communication. For example, these beams can introduce space-dependent optical torques, which is highly advantageous for optical manipulation in sorting and selecting particles and biomolecules. Such beams could also provide the possibility of creating the entanglement of varying quantum numbers along curved paths for quantum information processing and quantum computation.

4. Experimental Section

Numerical Simulations: The simulations shown in Figure 1 were conducted by using the finite-integration time-domain solver of the CST Microwave Studio software. In the simulation, periodic boundary conditions were employed along both x and y -directions in the unit cell. The permittivity of gold was taken from spectroscopic ellipsometry data fitted with a general oscillator model, and the refractive index of glass substrate was 1.45. The evolution process of TC inversion beam shown in Figure 3a,b was calculated by using the Fresnel–Kirchhoff diffraction integral

$$\Psi(x, y, z) = \frac{1}{i\lambda} \iint_S \Psi(x_0, y_0) \left[\frac{\cos(\mathbf{n}, \mathbf{r}) - \cos(\mathbf{n}, \mathbf{r}')}{2} \right] \frac{e^{ikr}}{r} dS \quad (8)$$

where $\Psi(x_0, y_0)$ is the complex amplitude distribution located at the $z = 0$ plane with surface area S and normal direction \mathbf{n} ; \mathbf{r}' is the vector between the source point and a point in the $z = 0$ plane, \mathbf{r} is the vector between the point in $z = 0$ plane and a point in the plane at the propagation distance z , and $k = 2\pi/\lambda$ is the wavevector. Since the Laguerre–Gaussian modes formed a complete Hilbert set, the OAM mode distributions of the TC inversion beam shown in Figure 4 were calculated by using the inner product between the vortex beam field and the Laguerre–Gaussian modes in Hilbert space.

Sample Fabrication: A 50 nm thick gold film was deposited on a glass substrate using electron-beam evaporation. Then the designed antenna arrays were milled in the gold film using FIB system (FEI Helios Nanolab 600, 30 kV, 9.7 pA). Two metasurface samples were fabricated to generate TC inversion beams. The metasurface sample to generate TC inversion beam along the straight line contained 150×150 unit cells, and the sample to generate self-accelerating TC inversion beam propagating along the parabolic trajectory contained 300×300 unit cells. Each unit cell contained a milled subwavelength nanoslit with size of $200 \text{ nm} \times 60 \text{ nm}$ at a specified orientation angle. According to the designed geometric phase profiles, the orientation angle for the nanoslit antenna in each unit cell was determined and used in the FIB fabrication of metasurface sample.

Optical Characterization: The transmission spectra through the metasurface sample under circular polarization basis shown in Figure 1d were measured with a collimated broadband Tungsten-Halogen source, where a combination of a linear polarizer and an achromatic quarter-wave plate was used to convert the incident light to circularly polarized wave. The light beam was focused normally onto

the sample using a $50\times$ objective lens and the transmitted light was collected by another $10\times$ objective lens to a spectrometer (Horiba, iHR 550). A transparent glass substrate was utilized to normalize the transmission spectra. Since the metasurface sample operated in a broad wavelength range from 600 to 1000 nm, three diode lasers operating at different wavelengths of 633, 808, and 988 nm were employed in the experiments. The intensity profiles and the interferometry patterns of TC inversion beams were captured by a microscope imaging system with a $20\times$ objective lens, a $0.5\times$ tube lens, and a CCD camera placed on a translation stage.

Acknowledgements

The authors acknowledge support from the Office of Naval Research under Grant No. N00014-16-1-2408 and the National Science Foundation under Grant Nos. ECCS-1653032 and DMR-1552871. The authors thank the facility support from the Materials Research Center at Missouri S&T.

Conflict of Interest

The authors declare no conflict of interest.

Keywords

geometric phase, metasurfaces, orbital angular momentum, plasmonic antennas, topological charge inversion

Received: October 30, 2018

Revised: January 11, 2019

Published online:

- [1] D. Grier, *Nature* **2003**, 424, 810.
- [2] S. Albaladejo, M. I. Marqués, M. Laroche, J. J. Sáenz, *Phys. Rev. Lett.* **2009**, 102, 113602.
- [3] M. Padgett, R. Bowman, *Nat. Photonics* **2011**, 5, 343.
- [4] J. Wang, J. Yang, I. M. Fazal, N. Ahmed, Y. Yan, H. Huang, Y. Ren, Y. Yue, S. Dolinar, M. Tur, A. E. Willner, *Nat. Photonics* **2012**, 6, 488.
- [5] P. J. Winzer, *Nat. Photonics* **2014**, 8, 345.
- [6] R. Fickler, R. Lapkiewicz, M. Huber, M. P. J. Lavery, M. J. Padgett, A. Zeilinger, *Nat. Commun.* **2014**, 5, 4502.
- [7] A. Nicolas, L. Veissier, L. Giner, E. Giacobino, D. Maxein, J. Laurat, *Nat. Photonics* **2014**, 8, 234.
- [8] B. C. Hiesmayr, M. J. A. De Dood, W. Löffler, *Phys. Rev. Lett.* **2016**, 116, 073601.
- [9] R. Fickler, R. Lapkiewicz, W. N. Plick, M. Krenn, C. Schaeff, S. Ramelow, A. Zeilinger, *Science* **2012**, 338, 640.
- [10] L. Marrucci, C. Manzo, D. Paparo, *Phys. Rev. Lett.* **2006**, 96, 163905.
- [11] Y. Zhao, J. S. Edgar, G. D. M. Jeffries, D. McGloin, D. T. Chiu, *Phys. Rev. Lett.* **2007**, 99, 073901.
- [12] K. P. Marzlin, W. Zhang, E. Wright, *Phys. Rev. Lett.* **1997**, 79, 4728.
- [13] Y. Tada, W. Nie, M. Oshikawa, *Phys. Rev. Lett.* **2015**, 114, 195301.
- [14] I. V. Basisti, V. Y. Bazhenov, M. S. Soskin, M. V. Vasnetsov, *Opt. Commun.* **1993**, 103, 422.
- [15] G. Molina-Terriza, J. P. Torres, L. Torner, E. M. Wright, *Phys. Rev. Lett.* **2001**, 87, 023902.
- [16] G. Molina-Terriza, E. M. Wright, L. Torner, *Opt. Lett.* **2001**, 26, 163.
- [17] A. V. Kildishev, A. Boltasseva, V. M. Shalae, *Science* **2013**, 339, 1232009.
- [18] N. Yu, F. Capasso, *Nat. Mater.* **2014**, 13, 139.

- [19] M. Jang, Y. Horie, A. Shibukawa, J. Brake, Y. Liu, S. M. Kamali, A. Arbabi, H. Ruan, A. Faraon, C. Yang, *Nat. Photonics* **2018**, *12*, 84.
- [20] M. Khorasaninejad, W. T. Chen, R. C. Devlin, J. Oh, A. Y. Zhu, F. Capasso, *Science* **2016**, *352*, 1190.
- [21] D. Lin, P. Fan, E. Hasman, M. L. Brongersma, *Science* **2014**, *345*, 298.
- [22] K. Ou, G. Li, T. Li, H. Yang, F. Yu, J. Chen, Z. Zhao, G. Cao, X. Chen, W. Lu, *Nanoscale* **2018**, *10*, 19154.
- [23] M. V. Berry, *J. Mod. Opt.* **1987**, *34*, 1401.
- [24] A. Niv, G. Biener, V. Kleiner, E. Hasman, *Opt. Express* **2006**, *14*, 4208.
- [25] E. Hasman, V. Kleiner, G. Biener, A. Niv, *Appl. Phys. Lett.* **2003**, *82*, 328.
- [26] M. Tymchenko, J. S. Gomez-Diaz, J. Lee, N. Nookala, M. A. Belkin, A. Alù, *Phys. Rev. Lett.* **2015**, *115*, 207403.
- [27] D. Zhang, X. Feng, K. Cui, F. Liu, Y. Huang, *Sci. Rep.* **2015**, *5*, 11982.
- [28] E. Karimi, S. A. Schulz, I. De Leon, H. Qassim, J. Upham, R. W. Boyd, *Light: Sci. Appl.* **2014**, *3*, e167.
- [29] J. Zeng, L. Li, X. Yang, J. Gao, *Nano Lett.* **2016**, *16*, 3101.
- [30] J. Zeng, T. S. Luk, J. Gao, X. Yang, *Sci. Rep.* **2017**, *7*, 11824.
- [31] Y. Liu, Y. Ke, J. Zhou, Y. Liu, H. Luo, S. Wen, D. Fan, *Sci. Rep.* **2017**, *7*, 44096.
- [32] F. Yue, D. Wen, J. Xin, B. D. Gerardot, J. Li, X. Chen, *ACS Photonics* **2016**, *3*, 1558.
- [33] K. Zhang, X. Ding, L. Zhang, Q. Wu, *New J. Phys.* **2014**, *16*, 103020.
- [34] K. Zhang, Y. Yuan, D. Zhang, X. Ding, B. Ratni, S. N. Burokur, M. Lu, K. Tang, Q. Wu, *Opt. Express* **2018**, *26*, 1351.
- [35] M. Khorasaninejad, W. T. Chen, A. Y. Zhu, J. Oh, R. C. Devlin, D. Rousso, F. Capasso, *Nano Lett.* **2016**, *16*, 4595.
- [36] X. Ni, S. Ishii, A. V. Kildishev, V. M. Shalaev, *Light: Sci. Appl.* **2013**, *2*, e72.
- [37] X. Chen, L. Huang, H. Mühlenbernd, G. Li, B. Bai, Q. Tan, G. Jin, C. Qiu, S. Zhang, T. Zentgraf, *Nat. Commun.* **2012**, *3*, 1198.
- [38] F. Aieta, P. Geneve, M. A. Kats, N. Yu, R. Blanchard, Z. Gaburro, F. Capasso, *Nano Lett.* **2012**, *12*, 4932.
- [39] N. Yu, F. Aieta, P. Geneve, M. A. Kats, Z. Gaburro, F. Capasso, *Nano Lett.* **2012**, *12*, 6328.
- [40] Y. Zhao, A. Alu, *Nano Lett.* **2013**, *13*, 1086.
- [41] W. Cao, X. Yang, J. Gao, *Sci. Rep.* **2017**, *7*, 8841.
- [42] H. Yang, G. Li, X. Su, G. Cao, Z. Zhao, F. Yu, X. Chen, W. Lu, *Opt. Express* **2017**, *25*, 16907.
- [43] W. Wan, J. Gao, X. Yang, *Adv. Opt. Mater.* **2017**, *5*, 1700541.
- [44] W. Wan, J. Gao, X. Yang, *ACS Nano* **2016**, *10*, 10671.
- [45] X. Ni, A. V. Kildishev, V. M. Shalaev, *Nat. Commun.* **2013**, *4*, 2807.
- [46] L. Huang, X. Chen, H. Mühlenbernd, H. Zhang, S. Chen, B. Bai, Q. Tan, G. Jin, K. Cheah, C. Qiu, J. Li, T. Zentgraf, S. Zhang, *Nat. Commun.* **2013**, *4*, 2808.
- [47] G. Zheng, H. Mühlenbernd, M. Kenney, G. Li, T. Zentgraf, S. Zhang, *Nat. Nanotechnol.* **2015**, *10*, 308.
- [48] G. Li, B. P. Clarke, J. So, K. F. MacDonald, N. I. Zheludev, *Nat. Commun.* **2016**, *7*, 13705.
- [49] I. D. Chremmos, Z. Chen, D. N. Christodoulides, N. K. Efremidis, *Opt. Lett.* **2012**, *37*, 5003.
- [50] A. Ferrando, M. Zcares, M. Garcia-March, J. A. Monsoriu, P. F. de Cordoba, *Phys. Rev. Lett.* **2005**, *95*, 123901.
- [51] P. Gregg, P. Kristensen, S. Ramachandran, *Optica* **2015**, *2*, 267.
- [52] C. Brunet, P. Vaity, Y. Messaddeq, S. LaRochelle, L. A. Rusch, *Opt. Express* **2014**, *22*, 26117.
- [53] J. A. Rodrigo, T. Alieva, E. Abramochkin, I. Castro, *Opt. Express* **2013**, *21*, 20544.
- [54] E. Greenfield, M. Segev, W. Walasik, O. Raz, *Phys. Rev. Lett.* **2011**, *106*, 213902.
- [55] G. A. Siviloglou, J. Broky, A. Dogariu, D. N. Christodoulides, *Phys. Rev. Lett.* **2007**, *99*, 213901.